

Magnetization Factors of Gamma-Ray Burst Jets Revealed by a Systematic Analysis of the Fermi Sample

AN LI,^{1,2} HE GAO,^{1,2} LIN LAN,³ AND BING ZHANG^{4,5}

¹*Institute for Frontier in Astronomy and Astrophysics, Beijing Normal University, Beijing 102206, China*

²*Department of Astronomy, Beijing Normal University, Beijing 100875, China*

³*CAS Key Laboratory of Space Astronomy and Technology, National Astronomical Observatories, Chinese Academy of Sciences, Beijing 100101, China*

⁴*Nevada Center for Astrophysics, University of Nevada Las Vegas, Las Vegas, NV 89154, USA*

⁵*Department of Physics and Astronomy, University of Nevada Las Vegas, Las Vegas, NV 89154, USA*

ABSTRACT

The composition of gamma-ray burst (GRB) jets remained a mystery until recently. In practice, we usually characterize the magnetization of the GRB jets (σ_0) through the ratio between the Poynting flux and matter (baryonic) flux. With the increasing value of σ_0 , magnetic energy gradually takes on a dominant role in the acceleration and energy dissipation of the jet, causing the proportion of thermal component in the prompt-emission spectrum of GRBs to gradually decrease or even be completely suppressed. In this work, we conducted an extensive analysis of the time-resolved spectrum for all *Fermi* GRBs with known redshift, and we diagnose σ_0 for each time bin by contrasting the thermal and nonthermal radiation components. Our results suggest that most GRB jets should contain a significant magnetic energy component, likely with magnetization factors $\sigma_0 \geq 10$. The value of σ_0 seems vary significantly within the same GRB. Future studies with more samples, especially those with lower-energy spectral information coverage, will further verify our results.

1. INTRODUCTION

After extensive research over the past 50 yr, substantial advancements have been achieved in comprehending gamma-ray bursts (GRBs; Zhang (2018)). Nonetheless, certain lingering questions persist, such as the exact proportion of magnetic energy within GRB jets.

In the very early picture, the magnetic field issue within GRB jets was not addressed, but rather it was assumed GRB outflows originate from an initially hot “fireball” composed of photons, electron/positron pairs and a small amount of baryons (Paczynski 1986; Goodman 1986; Shemi & Piran 1990). After an initially rapid acceleration phase under fireball thermal pressure, a significant fraction of the initial fireball thermal energy is converted to the kinetic energy of the jet (Meszaros et al. 1993; Piran et al. 1993). As the jet expands to the radius of the photosphere, the hot photons escape while the baryonic matter continues to expand to even greater distances, reconverting the kinetic energy into energetic particles through internal collisional dissipation (internal shock model; Rees & Meszaros 1994). Synchrotron (and possibly also synchrotron self-Compton) radiation by these particles gives rise to the observed nonthermal gamma-ray emission (Meszaros et al. 1994; Tavani 1996). In this scenario, the GRB spectrum is expected to consist of a combination of thermal and nonthermal components.

Equipped with both the Gamma-ray Burst Monitor (GBM; Meegan et al. 2009) and the Large Area Telescope (Atwood et al. 2009), Fermi spacecraft broadened the observational range to cover 6-7 orders of magnitude in energy, thereby having a considerable advantage for a comprehensive study of spectral components within the prompt emission spectra of GRBs. Based on the Fermi sample, one speculation of the synthesized prompt emission spectrum for GRBs has been established, which may include three elemental spectral components (Zhang et al. 2011): (I) a nonthermal band component; (II) a quasithermal component; and (III) another nonthermal component extending to high energies,

and the significance of different spectral components may vary among different GRBs. These results have also been confirmed by other satellite data, such as Compton Gamma Ray Observatory/BATSE data (Guiriec et al. 2016a).

After more than a decade of observations, *Fermi* has detected a population of GRBs that exhibit pure nonthermal spectra across several orders of magnitude in energy (Abdo et al. 2009a; Zhang et al. 2011). The absence of photospheric emission poses a significant challenge to the “fireball” model (Zhang & Yan 2011). One solution to solve this problem is that GRB outflows should contain certain proportion of magnetic energy so that the contribution of the thermal component can be significantly reduced (Daigne & Mochkovitch 2002; Zhang & Pe’er 2009; Zhang & Yan 2011; Lazarian et al. 2019). In this case, the total luminosity of GRB jets can be decomposed into the sum of the luminosity from hot components (L_h) and the luminosity from cold (Poynting flux) components (L_c), where the magnetization parameter at the central engine σ_0 can be defined as

$$\sigma_0 \equiv \frac{L_{c,0}}{L_{h,0}}. \quad (1)$$

In a hybrid jet scenario (Gao & Zhang 2015), if $\sigma_0 \ll 1$, one gets back to a hot fireball. With the increasing value of σ_0 , magnetic energy gradually takes on a dominant role in the acceleration and energy dissipation of the jet, causing the nonthermal radiation component associated with magnetic dissipation to become stronger compared to the thermal radiation component. For moderate values of σ_0 , thermal radiation becomes subdominant. For extremely large values of σ_0 , the thermal component is completely suppressed, and only featureless nonthermal radiation can be observed.

From an observational perspective, we do have sources whose spectrum are dominated by thermal components (Abdo et al. 2009b), which should correspond to $\sigma_0 \ll 1$; we also have cases where the thermal component is subdominant, (Guiriec et al. 2011, 2013, 2015b,a, 2016a,b, 2017; Axelsson et al. 2012; Burgess et al. 2014; Preece et al. 2014), which should correspond to moderate values of σ_0 . The most prevalent cases are sources with featureless nonthermal radiation, which are expected to have extremely large values of σ_0 (Abdo et al. 2009a; Zhang et al. 2011).

From a theoretical perspective, Gao & Zhang (2015) developed an analytical method to quantify the spectrum properties for a hybrid GRB jet with both a hot fireball component and a cold Poynting flux component. They developed (1) a “bottom-up” approach to predict the temperature and luminosity of the photosphere emission for an arbitrary value of σ_0 ; (2) a “top-down” approach to diagnose σ_0 using the observational quantities of the energy spectrum, especially by contrasting the thermal and nonthermal radiation components. Many studies have used this method to successfully explain specific GRBs that show a superposed thermal component in the spectra,¹ such as GRB 110721A (Iyyani et al. 2016), GRB 130310A (Qin et al. 2021), GRB 130518A (Siddique et al. 2022), GRB 211211A (Chang et al. 2023).

In this paper, we intend to systematically apply this method (the “top-down” approach) to a large sample of GRBs observed by *Fermi*, estimating the exact value of σ_0 for bursts with a superposed thermal component or the lower limit of σ_0 for bursts with a featureless nonthermal component. Eventually, we plan to obtain the distribution of σ_0 for all the samples, enabling us to conduct a comprehensive investigation and gain insights into the various constituents comprising the GRB jet.

2. DATA REDUCTION AND SAMPLE SELECTION

In this work, we use the data observed by the *Fermi* GBM, which is downloaded from the Fermi Science Support Center’s FTP site² and processed with GBM data tools v1.1.1. 3359 GRBs were detected by *Fermi*/GBM up to 2022 August 1. We use time-tagged event (TTE) data and response (RSP or RSP2) files for spectral analysis and simulation. The TTE data file records each photon’s arrival time with 2 μ s temporal resolution and which of the 128 energy channels the photon registered. The RSP file records the response matrix of the detector at the trigger time. The RSP2 file records a time sequence of response matrices around the trigger point; it is used when the spectrum slice is significantly distant from the trigger time, making the response matrix in the RSP file inapplicable.

The GBM consists of two sets of detectors: 12 sodium iodide (NaI) scintillators sensitive to the lower end of the energy range and two cylindrical bismuth germanate (BGO) scintillators sensitive to the higher energy range. For the data sample, we selected two of the strongest triggered TTE data files from the NaI detectors, covering the energy range from 8 to 900 keV, and the strongest triggered TTE data file from the BGO detectors, covering the energy range from 500 keV to 30 MeV. Each TTE data file is accompanied by a corresponding calibration file.

¹ There are also works applying similar methods to Gao & Zhang (2015), which theoretically explained individual sources with thermal and nonthermal superposed spectra and constrained their magnetization factors, e.g. GRB 100724B (Guiriec et al. 2011) and GRB 130323A (Guiriec et al. 2013).

² <https://heasarc.gsfc.nasa.gov/FTP/fermi/>

For the purpose of this study, an initial screening of the data sample was conducted based on two criteria: (1) availability of redshift information, as the calculation method of σ_0 requires the redshift of the source; and (2) the signal-to-noise ratio (SNR) within the T_{90} range higher than 30. This criterion ensures sufficient photon counts for credible results. The SNR calculation equation is as follows:

$$\text{SNR} = \frac{N_{\text{all}} - N_{\text{bak}}}{\sqrt{N_{\text{bak}}}}, \quad (2)$$

where N_{all} represents the photon counts within the source time range, including both source and background photon counts. The background photon counts, N_{bak} , are estimated using background trends outside the T_{90} time range via polynomial interpolation. Ultimately, 87 GRBs were selected for further analysis.

Given the evolving nature of central engine properties, the value of σ_0 might vary at different stages of GRB prompt emission. Therefore, utilizing time-resolved spectra with the smallest possible time bin is crucial for accurately constraining σ_0 . For the selected sample, each source was binned based on a criterion of an SNR higher than 30, consistent with the selection criteria above. Additionally, we recognized that relying solely on SNR for defining time intervals may lead to mixing peaks and valleys of the light curves at different energies. To address this, during the selection of time intervals for each source, a manual review was conducted, and if necessary, manual adjustments were made to avoid this issue. Consequently, a total of 87 GRBs were divided into 318 slices (see Table 1 for details).

We then fit each slice with three different spectral models: nonthermal, hybrid (nonthermal + thermal), and thermal. For the nonthermal spectrum, we adopt either cutoff power-law (“CPL” in the table) function or Band function (“Band” in the table; Band et al. 1993), which can be expressed as

$$F(E) = Ae^{-(2+\alpha)E/E_{\text{peak}}}\left(\frac{E}{100 \text{ keV}}\right)^\alpha, \quad (3)$$

and

$$F(E) = \begin{cases} A\left(\frac{E}{100 \text{ keV}}\right)^\alpha e^{-(2+\alpha)E/E_{\text{peak}}}, & \text{if } E < \frac{(\alpha-\beta)E_{\text{peak}}}{2+\alpha}, \\ A\left(\frac{(\alpha-\beta)E_{\text{peak}}}{(2+\alpha)100 \text{ keV}}\right)^{\alpha-\beta} e^{\beta-\alpha}\left(\frac{E}{100 \text{ keV}}\right)^\beta, & \text{otherwise} \end{cases} \quad (4)$$

respectively, where α and β are low-energy and high-energy photon spectral indices, respectively. E_{peak} is the $\nu F\nu$ peak in keV.

For the hybrid spectrum, we combined nonthermal spectral function with a blackbody function (“BB” in the talbe) described as follows:

$$F(E) = A\frac{E^2}{e^{E/kT} - 1} \quad (5)$$

where kT is the temperature in unit of keV.

For the thermal spectrum, we adopt the multicolour blackbody model (Pe’er et al. 2012), which can be described as (Hou et al. 2018) :

$$N(E) = \frac{8.0525(m+1)K}{\left(\frac{T_{\text{max}}}{T_{\text{min}}}\right)^{m+1} - 1} \left(\frac{kT_{\text{min}}}{\text{keV}}\right)^{-2} I(E), \quad (6)$$

$$I(E) = \left(\frac{E}{kT_{\text{min}}}\right)^{m-1} \int_{\frac{E}{kT_{\text{min}}}}^{\frac{E}{kT_{\text{max}}}} \frac{x^{2-m}}{e^x - 1} dx$$

where kT is the temperature in unit of keV. The spectrum consists of a superposition of Planck functions in the temperature range from T_{min} to T_{max} . m is the power-law index of the Planck functions’ distribution.

Here we use the Bayesian information criterion (BIC) to determine the best-fitting model. The BIC is a criterion used to evaluate the best-fitting model from a finite set of models, where the model with the lowest BIC value is considered preferred. The BIC can be defined as follows: $\text{BIC} = -2 \ln L + k \ln(n)$, where k represents the number of model parameters, n is the number of data points, and L is the maximum value of the likelihood function for the estimated model.

Eventually, we have 225 slices (in 55 GRBs) that display a featureless nonthermal spectrum, 81 slices (in 30 GRBs) that display a hybrid spectrum and only 12 slices (in GRB 090902B and GRB 210610B) that display a multicolour blackbody spectrum. For all 318 slices, the best-fitting models are collected in Table 1 with their parameters.

3. σ_0 ESTIMATION

The fundamental properties of a GRB jet can be characterized by a series of parameters, including the initial radius (r_0) at which the jet emanates from the central engine, the total luminosity ($L_{w,0}$) of the jet, the dimensionless entropy (η) that defines average total energy (rest-mass energy plus thermal energy) per baryon in the hot component, and the magnetization parameter at the central engine (σ_0). After leaving the central engine, the jet will continuously expand and accelerate under the combined effects of thermal pressure and magnetic pressure until it reaches its maximum velocity $\Gamma_c \simeq \eta(1 + \sigma_0)$ at the coasting radius r_c . After the jet exceeds a radius of r_{ph} , the photon optical depth for Thomson scattering drops below unity so that photons previously trapped in the jet can escape. The observed temperature and flux for the photosphere emission are essentially determined by the temperature at r_0 , which reads

$$T_0 \simeq \left(\frac{L_w}{4\pi r_0^2 a c (1 + \sigma_0)} \right)^{1/4}, \quad (7)$$

where $a = 7.56 \times 10^{-15} \text{ erg cm}^{-3} \text{ K}^{-4}$ is the radiation density constant and by the position of the photosphere, namely, whether the photospheric emission occurs during the acceleration phase or the coasting phase of the jet. Based on the relative magnitudes of η and σ_0 , as well as the different relationships between r_{ph} and r_c , [Gao & Zhang \(2015\)](#) divided the parameter space of the central engine into different regimes:³ (I) $\eta > (1 + \sigma_0)^{1/2}$ and $r_{\text{ph}} < r_c$; (II) $\eta > (1 + \sigma_0)^{1/2}$ and $r_{\text{ph}} > r_c$; (III) $\eta < (1 + \sigma_0)^{1/2}$ and $r_{\text{ph}} < r_c$; and (IV) $\eta < (1 + \sigma_0)^{1/2}$ and $r_{\text{ph}} > r_c$. For each regime, [Gao & Zhang \(2015\)](#) developed an analytical method to connect the observed quantities of GRB spectrum with the central engine parameters; for instance, they find that

$$1 + \sigma_0 = \begin{cases} 25.5(1+z)^{4/3} \left(\frac{kT_{\text{ob}}}{50\text{keV}} \right)^{4/3} \left(\frac{F_{\text{BB}}}{10^{-8}\text{erg s}^{-1}\text{cm}^{-2}} \right)^{-1/3} r_{0,9}^{2/3} f_{\text{th},-1}^{-1} f_{\gamma}^{-1} d_{L,28}^{-2/3}, & \text{Regime I} \\ 5.99(1+z)^{4/3} \left(\frac{kT_{\text{ob}}}{30\text{keV}} \right)^{4/3} \left(\frac{F_{\text{BB}}}{10^{-7}\text{erg s}^{-1}\text{cm}^{-2}} \right)^{-1/3} r_{0,9}^{2/3} f_{\text{th},-1}^{-1} f_{\gamma}^{-1} d_{L,28}^{-2/3}, & \text{Regime II and III} \\ 6.43(1+z)^{4/3} \left(\frac{kT_{\text{ob}}}{10\text{keV}} \right)^{4/3} \left(\frac{F_{\text{BB}}}{10^{-9}\text{erg s}^{-1}\text{cm}^{-2}} \right)^{-1/3} r_{0,9}^{2/3} f_{\text{th},-1}^{-1} f_{\gamma}^{-1} d_{L,28}^{-2/3}, & \text{Regime IV} \end{cases} \quad (8)$$

where T_{ob} is the observed blackbody temperature and F_{BB} is the observed blackbody flux. f_{th} is defined as $F_{\text{BB}}/F_{\text{ob}}$, where F_{ob} is the observed total flux (both thermal and nonthermal included). $f_{\gamma} = L_{\gamma}/L_w$, which connects the total flux F_{ob} to the wind luminosity L_w . The L_w is estimated by $L_w = 4\pi d_L^2 F_{\text{ob}}/f_{\gamma}$, in which d_L is the luminosity distance of the GRB.

Here we use the method proposed in [Gao & Zhang \(2015\)](#) to estimate the value of σ_0 for our selected sample. For slices that display a multicolour blackbody spectrum, we set their σ_0 equal to 0. For slices that display a hybrid spectrum, we first extract the observed quantities such as T_{ob} , F_{BB} and f_{th} by fitting the spectrum. With these observed quantities, we can determine which regime these slices fall into by using the judgment criteria provided in Table 2 (see also Table 1 and 2 in [Gao & Zhang \(2015\)](#)). Then, we can use Equation 8 to calculate the corresponding σ_0 for these slices. The results are shown in Figure 1 and Table 1. It is worth noting that in our estimation, we fix f_{γ} to be a typical value of 0.5, and we consider three r_0 values: 10^8cm , 10^9cm , and 10^{10}cm .

For slices with a featureless nonthermal component, we adopted the following approach to estimate their lower limit of σ_0 :

- For each slice, we first assume that its thermal component corresponds to a temperature of kT , with kT starting at 5 keV.
- For a given kT , we assume a series of ratios of thermal component flux to nonthermal component flux (f_{th}), with f_{th} values starting at 0.005 and increasing with equal steps (0.1 dex) on a log scale.
- For each pair of kT and f_{th} , we use the same response file as the original data to simulate the corresponding thermal component photons with random noise through the GBM data tools ([Goldstein et al. 2022](#)).
- We add these simulated photons to the original data, reperform spectral fitting, and compare the BIC results of the featureless nonthermal spectrum with the hybrid spectrum. If the nonthermal spectrum is the best fit,

³ The jet undergoes a rapid acceleration phase initially with $\Gamma \propto r$ until reaching the radius of r_{ra} , which is defined by the larger one of the thermal coasting radius and the magnetosonic point. In [Gao & Zhang \(2015\)](#), two extreme regimes with $r_{\text{ph}} < r_{\text{ra}}$ are also discussed. We do not consider these extreme scenarios here since they introduce an additional degeneracy so that central engine parameters cannot be inferred from observations.

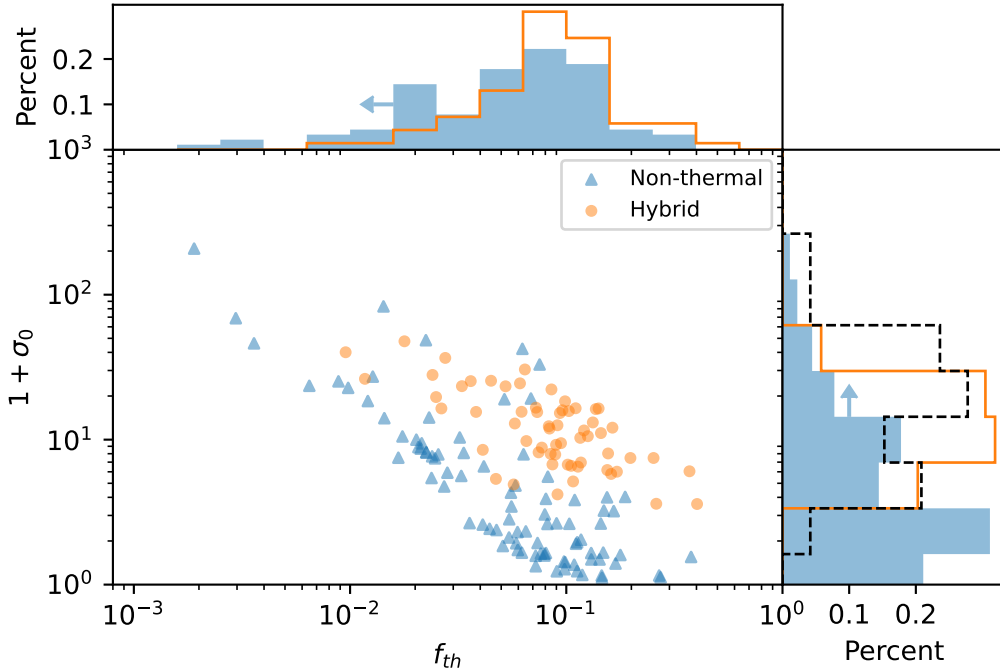


Figure 1. Distribution plot of $1 + \sigma_0$ and f_{th} . The blue triangles represent the lower limit of $1 + \sigma_0$ for slices with non-thermal spectrum, the orange points represent the value of $1 + \sigma_0$ for slices with hybrid spectrum. The black dashed line in the sub figure represents the distribution result of $1 + \sigma_0$ taken from Li (2019). The results shown in this figure are based on the same r_0 value as 10^9 cm.

we continue to increase the f_{th} value and resimulate more thermal photons until the hybrid spectrum becomes dominant. This way, we have found the upper limit of f_{th} for a given kT .

- Taking kT and the upper limit of f_{th} as the observed quantities, we use the judgment criteria provided in Table 2 and equations 8 to calculate the corresponding σ_0 , which could be taken as the lower limit of σ_0 corresponding to kT .
- We continuously increase the assumed value of kT (from 5 keV to 60 keV with a uniform step size of 5 keV), calculate the corresponding lower limit of σ_0 for each kT using the methods above, and take the minimum value of all the lower limits as the overall lower limit of σ_0 for this slice.

In Figure 1, we show the distribution plot of $1 + \sigma_0$ vs. f_{th} for all slices with both nonthermal and hybrid spectra. For the hybrid slice, we find that $1 + \sigma_0$ values are distributed in the range of 3.6-47.7, and if fitted with a Gaussian function, its peak is at 11.9 with a variance of 0.3. On the other hand, f_{th} is distributed in the range of 0.009-0.4, and if fitted with a Gaussian function on a log scale, its peak is at 0.08 with a variance of 0.3. Also, we show the distribution plot of $1 + \sigma_0$ lower limit vs. f_{th} upper limit for all slices with a featureless nonthermal spectrum. We find that the $1 + \sigma_0$ lower limits are distributed in the range of 1.1-424.9, with $\sim 23\%$ larger than 10. The f_{th} upper limits are distributed in the range of 0.003-0.4.

As shown in Figure 2, we find that the values of kT_{ob} for all slices with the hybrid spectrum are distributed in the range of 8.5-58.7 keV, with the average value located at 28.4 keV with a variance of 10.5 keV.

4. CONCLUSION AND DISCUSSION

In this study, we conducted an extensive analysis of the magnetic component within GRBs observed by the Fermi satellite. Our focus was on GRB data with known redshift, and we employed a time-resolved approach to determine the parameter σ_0 for each time bin. We categorized the GRBs into three distinct groups based on their dominant spectral components and applied different processing procedures for each:

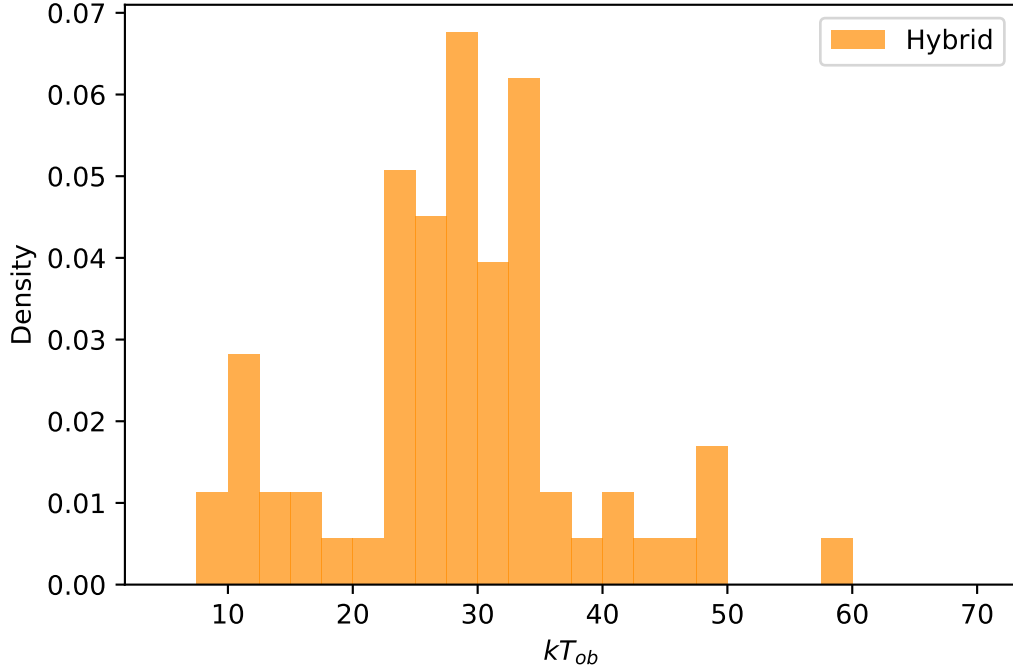


Figure 2. The distribution of kT_{ob} in the GRB with hybrid spectrum.

- Thermal-dominant spectra: in the case of 12 slices with thermal-dominant spectra, we set their σ_0 equal to 0.
- Hybrid spectra: we have 81 slices with hybrid spectra, for which we calculated their σ_0 values based on the extracted quantities such as T_{ob} , F_{BB} and f_{th} by fitting the spectrum.
- Nonthermal spectra: we have 225 slices with nonthermal spectra, for which we estimate the lower limit of their σ_0 value by simulating the upper limit of the thermal component.

We find that for all slices with the hybrid spectrum, the values of kT_{ob} are distributed around 28 keV with a variance of 11 keV, and the values of f_{th} are distributed around 0.08 with a variance of 0.3 on a log scale. In this case, their $1 + \sigma_0$ values should be distributed around 11.9 with a variance of 0.3 on a log scale. These results are consistent with previous results obtained by using a limited number of specific GRBs (Zhang & Pe'er 2009; Guiriec et al. 2011; Iyyani et al. 2013; Li 2019; Chang et al. 2023). On the other hand, we find that for all slices with the featureless nonthermal spectrum, the $1 + \sigma_0$ lower limits are distributed in the range of 1.1-424.9, with 22.7% larger than 10.

Our results suggest that most GRB jets should contain a significant magnetic energy component, likely with magnetization factors $\sigma_0 \geq 10$. In this case, the prompt emission mainly arises from magnetized dissipation in such highly magnetized environments as particle acceleration via internal shocks is suppressed. With detailed analysis of a small number of sources that show hybrid spectra in multiple slices, we find that the value of σ_0 varies significantly within the same GRB. In Figure 3, we present three examples (GRB 171010A, GRB 211211A, and GRB 130427A) that best reflect the evolution of σ_0 . These examples are selected because they have thermal components in three or more consecutive time bins. The evolution trend of σ_0 does not show an obvious relationship with those of lightcurve and E_{peak} .

We would like to point out that we have only considered the case where kT varies from 5 to 60 keV when constraining the lower limit of the magnetization factor for the nonthermal spectra. The reasons are (1) the SNR of Fermi/GBM observations below 5 keV is too low to perform a good spectral fitting; and (2) according to the fitting results of the hybrid spectra slices, there are almost no cases where kT is greater than 60 keV. For these nonthermal spectra, if their true kT is greater than 60 keV, then the corresponding lower limit of the magnetization factor should be higher than our current results, which would further support our conclusion that GRB jets have high magnetization.

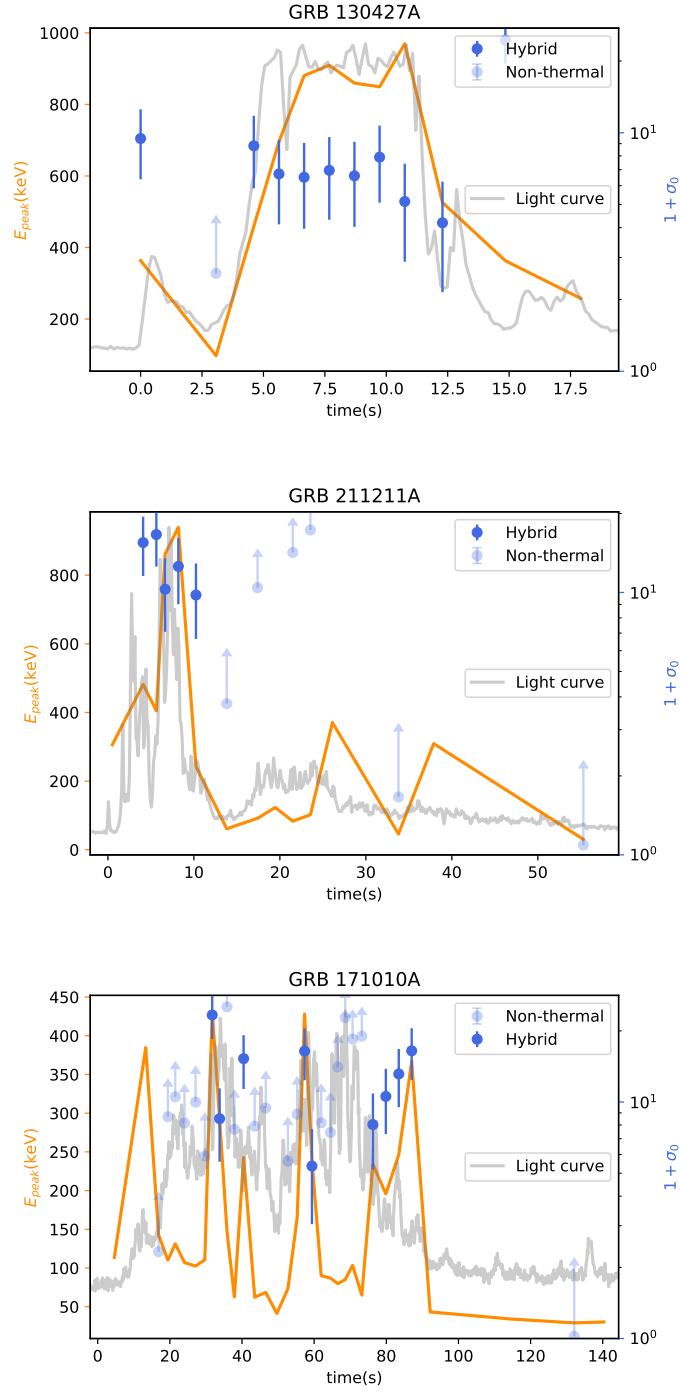


Figure 3. Evolution of photon counts, $1 + \sigma_0$ and E_{peak} , for sources that show hybrid spectra in multiple slices.

However, if the true kT is lower than 5 keV, then our current constraint on the lower limit of the magnetization factor may be overestimated to a certain extent. However, this uncertainty should be within a factor of 2. In the future, instruments like Fermi, Gravitational Wave High-energy Electromagnetic Counterpart All-sky Monitor, Einstein Probe (Yuan et al. 2018) and Space Variable Objects Monitor (Wei et al. 2016) are expected to form an observation network in a broadband and provide high-quality GRB data during the prompt emission and early-afterglow phases through joint analysis, which would significantly enhance the accuracy of our results.

Previous studies have indicated that if a more complex model is used to fit the energy spectrum, some slices that originally satisfy the pure nonthermal spectrum may show weaker evidence of the existence of a thermal spectrum (e.g., GRB 080916C and GRB 090926A; see Guiriec et al. (2016a) for details). The fitting of the energy spectrum performed here does not include such complexity. However, it is important to emphasize that the lower limit of σ_0 given by the pure nonthermal spectrum in this study is the most conservative constraint. If thermal components are indeed missed, the constraint on σ_0 brought by these thermal components will definitely be above the lower limit we have provided, which would further strengthen our conclusion that GRB jets generally possess high magnetization.

Finally, we note that the low-energy end of the BGO detector was excluded from the analysis due to its low SNR. To ensure proper calibration between the NaI and BGO detectors, we also conducted analysis by including the low-energy end of the BGO data (e.g. over the energy range from 300 keV to 30 MeV), and we found that our main results were barely affected.

ACKNOWLEDGMENTS

We gratefully acknowledge the insightful comments provided by the anonymous referee and Asaf Pe'er. This work is supported by the National Natural Science Foundation of China (Projects 12373040,12021003), the National SKA Program of China (2022SKA0130100), the National Postdoctoral Program for Innovative Talents (grant No. GZB20230765) and the Fundamental Research Funds for the Central Universities.

Facilities: Fermi(GBM)

Software: `astropy` Astropy Collaboration et al. (2013), GBM data tools Goldstein et al. (2022)

REFERENCES

- Abdo, A. A., Ackermann, M., Arimoto, M., et al. 2009a, *Science*, 323, 1688, doi: [10.1126/science.1169101](https://doi.org/10.1126/science.1169101)
- Abdo, A. A., Ackermann, M., Ajello, M., et al. 2009b, *ApJL*, 706, L138, doi: [10.1088/0004-637X/706/1/L138](https://doi.org/10.1088/0004-637X/706/1/L138)
- Astropy Collaboration, Robitaille, T. P., Tollerud, E. J., et al. 2013, *A&A*, 558, A33, doi: [10.1051/0004-6361/201322068](https://doi.org/10.1051/0004-6361/201322068)
- Atwood, W. B., Abdo, A. A., Ackermann, M., et al. 2009, *ApJ*, 697, 1071, doi: [10.1088/0004-637X/697/2/1071](https://doi.org/10.1088/0004-637X/697/2/1071)
- Axelsson, M., Baldini, L., Barbiellini, G., et al. 2012, *ApJL*, 757, L31, doi: [10.1088/2041-8205/757/2/L31](https://doi.org/10.1088/2041-8205/757/2/L31)
- Band, D., Matteson, J., Ford, L., et al. 1993, *The Astrophysical Journal*, 413, 281, doi: [10.1086/172995](https://doi.org/10.1086/172995)
- Burgess, J. M., Preece, R. D., Connaughton, V., et al. 2014, *ApJ*, 784, 17, doi: [10.1088/0004-637X/784/1/17](https://doi.org/10.1088/0004-637X/784/1/17)
- Chang, X.-Z., Lü, H.-J., Yang, X., Chen, J.-M., & Liang, E.-W. 2023, *The Astrophysical Journal*, 943, 146, doi: [10.3847/1538-4357/aca969](https://doi.org/10.3847/1538-4357/aca969)
- Daigne, F., & Mochkovitch, R. 2002, *MNRAS*, 336, 1271, doi: [10.1046/j.1365-8711.2002.05875.x](https://doi.org/10.1046/j.1365-8711.2002.05875.x)
- Gao, H., & Zhang, B. 2015, *ApJ*, 801, 103, doi: [10.1088/0004-637X/801/2/103](https://doi.org/10.1088/0004-637X/801/2/103)
- Goldstein, A., Cleveland, W. H., & Kocevski, D. 2022, *Fermi GBM Data Tools: v1.1.1*. <https://fermi.gsfc.nasa.gov/ssc/data/analysis/gbm>
- Goodman, J. 1986, *ApJL*, 308, L47, doi: [10.1086/184741](https://doi.org/10.1086/184741)
- Guiriec, S., Gehrels, N., McEnery, J., Kouveliotou, C., & Hartmann, D. H. 2017, *ApJ*, 846, 138, doi: [10.3847/1538-4357/aa81c2](https://doi.org/10.3847/1538-4357/aa81c2)
- Guiriec, S., Gonzalez, M. M., Sacahui, J. R., et al. 2016a, *ApJ*, 819, 79, doi: [10.3847/0004-637X/819/1/79](https://doi.org/10.3847/0004-637X/819/1/79)
- Guiriec, S., Mochkovitch, R., Piran, T., et al. 2015a, *ApJ*, 814, 10, doi: [10.1088/0004-637X/814/1/10](https://doi.org/10.1088/0004-637X/814/1/10)
- Guiriec, S., Connaughton, V., Briggs, M. S., et al. 2011, *ApJL*, 727, L33, doi: [10.1088/2041-8205/727/2/L33](https://doi.org/10.1088/2041-8205/727/2/L33)
- Guiriec, S., Connaughton, V., Briggs, M., et al. 2011, 33, doi: [10.1063/1.3621732](https://doi.org/10.1063/1.3621732)
- Guiriec, S., Daigne, F., Hascoët, R., et al. 2013, *ApJ*, 770, 32, doi: [10.1088/0004-637X/770/1/32](https://doi.org/10.1088/0004-637X/770/1/32)
- Guiriec, S., Kouveliotou, C., Daigne, F., et al. 2015b, *ApJ*, 807, 148, doi: [10.1088/0004-637X/807/2/148](https://doi.org/10.1088/0004-637X/807/2/148)
- Guiriec, S., Kouveliotou, C., Hartmann, D. H., et al. 2016b, *ApJL*, 831, L8, doi: [10.3847/2041-8205/831/1/L8](https://doi.org/10.3847/2041-8205/831/1/L8)
- Hou, S.-J., Zhang, B.-B., Meng, Y.-Z., et al. 2018, *ApJ*, 866, 13, doi: [10.3847/1538-4357/aadc07](https://doi.org/10.3847/1538-4357/aadc07)
- Iyyani, S., Ryde, F., Burgess, J., Pe'er, A., & Bégué, D. 2016, *Monthly Notices of the Royal Astronomical Society*, 456, 2157, doi: [10.1093/mnras/stv2751](https://doi.org/10.1093/mnras/stv2751)

- Iyyani, S., Ryde, F., Axelsson, M., et al. 2013, *Monthly Notices of the Royal Astronomical Society*, 433, 2739, doi: [10.1093/mnras/stt863](https://doi.org/10.1093/mnras/stt863)
- Lazarian, A., Zhang, B., & Xu, S. 2019, *ApJ*, 882, 184, doi: [10.3847/1538-4357/ab2b38](https://doi.org/10.3847/1538-4357/ab2b38)
- Li, L. 2019, *The Astrophysical Journal Supplement Series*, 245, 7, doi: [10.3847/1538-4365/ab42de](https://doi.org/10.3847/1538-4365/ab42de)
- Meegan, C., Lichti, G., Bhat, P. N., et al. 2009, *ApJ*, 702, 791, doi: [10.1088/0004-637X/702/1/791](https://doi.org/10.1088/0004-637X/702/1/791)
- Meszáros, P., Laguna, P., & Rees, M. J. 1993, *ApJ*, 415, 181, doi: [10.1086/173154](https://doi.org/10.1086/173154)
- Meszáros, P., Rees, M. J., & Papathanassiou, H. 1994, *ApJ*, 432, 181, doi: [10.1086/174559](https://doi.org/10.1086/174559)
- Paczynski, B. 1986, *The Astrophysical Journal*, 308, L43, doi: [10.1086/184740](https://doi.org/10.1086/184740)
- Pe'er, A., Zhang, B.-B., Ryde, F., et al. 2012, *Monthly Notices of the Royal Astronomical Society*, 420, 468, doi: [10.1111/j.1365-2966.2011.20052.x](https://doi.org/10.1111/j.1365-2966.2011.20052.x)
- Piran, T., Shemi, A., & Narayan, R. 1993, *MNRAS*, 263, 861, doi: [10.1093/mnras/263.4.861](https://doi.org/10.1093/mnras/263.4.861)
- Preece, R., Burgess, J. M., von Kienlin, A., et al. 2014, *Science*, 343, 51, doi: [10.1126/science.1242302](https://doi.org/10.1126/science.1242302)
- Qin, S.-M., Jiang, L.-Y., & Wang, X.-G. 2021, *Research in Astronomy and Astrophysics*, 21, 072, doi: [10.1088/1674-4527/21/3/72](https://doi.org/10.1088/1674-4527/21/3/72)
- Rees, M. J., & Meszáros, P. 1994, *ApJL*, 430, L93, doi: [10.1086/187446](https://doi.org/10.1086/187446)
- Shemi, A., & Piran, T. 1990, *ApJL*, 365, L55, doi: [10.1086/185887](https://doi.org/10.1086/185887)
- Siddique, I., Sajjad, S., & Motiwala, K. 2022, *The Astrophysical Journal*, 938, 159, doi: [10.3847/1538-4357/ac8d05](https://doi.org/10.3847/1538-4357/ac8d05)
- Tavani, M. 1996, *ApJ*, 466, 768, doi: [10.1086/177551](https://doi.org/10.1086/177551)
- Wei, J., Cordier, B., Antier, S., et al. 2016, *arXiv e-prints*, arXiv:1610.06892, doi: [10.48550/arXiv.1610.06892](https://doi.org/10.48550/arXiv.1610.06892)
- Yuan, W., Zhang, C., Ling, Z., et al. 2018, in *Society of Photo-Optical Instrumentation Engineers (SPIE) Conference Series*, Vol. 10699, *Space Telescopes and Instrumentation 2018: Ultraviolet to Gamma Ray*, ed. J.-W. A. den Herder, S. Nikzad, & K. Nakazawa, 1069925, doi: [10.1117/12.2313358](https://doi.org/10.1117/12.2313358)
- Zhang, B. 2018, *The Physics of Gamma-Ray Bursts* (Cambridge University Press), doi: [10.1017/9781139226530](https://doi.org/10.1017/9781139226530)
- Zhang, B., & Pe'er, A. 2009, *ApJL*, 700, L65, doi: [10.1088/0004-637X/700/2/L65](https://doi.org/10.1088/0004-637X/700/2/L65)
- Zhang, B., & Yan, H. 2011, *The Astrophysical Journal*, 726, 90, doi: [10.1088/0004-637X/726/2/90](https://doi.org/10.1088/0004-637X/726/2/90)
- Zhang, B.-B., Zhang, B., Liang, E.-W., et al. 2011, *ApJ*, 730, 141, doi: [10.1088/0004-637X/730/2/141](https://doi.org/10.1088/0004-637X/730/2/141)

Table 1. σ_0 constraint result

Burst Name	Start Time($T_0 + s$)	End Time($T_0 + s$)	Fit Model	E_{peak} (keV)	kT (keV)	f_{th}	$1 + \sigma_0$		
							$r_{0,1}^1$	$r_{0,2}^1$	$r_{0,3}^1$
GRB080804A	-2.048	15.360	CPL+BB	209.948	26.682	0.1980	1.609	7.472	-
GRB080810A	-2.048	22.528	CPL	4265.090	5.000	0.3020	-	-	2.314
GRB080916C	-2.048	15.360	Band	149.793	5.000	0.3546	-	-	1.840
GRB081121A	-2.048	16.384	Band	129.227	5.000	0.1781	-	-	3.719
GRB081221A	20.480	24.576	CPL	123.083	20.000	0.4317	-	-	4.529
GRB081222A	-2.048	6.144	Band	147.967	5.000	0.1218	-	1.189	5.524
	6.144	14.336	Band	77.290	5.000	0.5013	-	-	1.004
GRB090102A	10.240	19.456	Band	1130.951	5.000	0.1575	-	-	3.349
GRB090323A	-2.048	26.624	Band+BB	261.177	33.910	0.1369	3.500	16.257	-
	26.624	53.248	Band	1060.073	5.000	0.1458	-	1.155	5.367
	53.248	64.512	Band	1021.761	5.000	0.1446	-	-	4.049
GRB090328A	-2.048	14.336	Band	581.272	5.000	0.1686	-	-	3.807
	14.336	23.552	Band	1287.037	5.000	0.1740	-	-	3.038
	23.552	38.912	Band	545.817	5.000	0.3475	-	-	1.521
GRB090424A	-2.048	2.048	Band	67.578	5.000	0.0595	-	2.303	10.698
	2.048	5.120	Band+BB	268.941	9.271	0.0563	1.057	4.906	22.788
GRB090510A	0.000	1.000	CPL	3864	50.000	0.0753	7.107	32.986	-
GRB090516A	-7.168	19.456	Band	4287.681	5.000	0.3353	-	-	2.420
GRB090618A	48.128	60.416	Band	130.992	10.000	0.4676	-	-	2.308
	60.416	64.512	Band	413.189	5.000	0.0611	-	1.853	8.607
	64.512	67.584	Band	156.887	5.000	0.0476	-	2.379	11.049
	67.584	70.656	Band	108.743	5.000	0.0587	-	1.930	8.964
	70.656	74.752	Band	70.328	20.000	0.1295	1.109	5.153	-
	74.752	79.872	Band+BB	286.238	23.984	0.1694	1.297	6.026	-
	79.872	83.968	Band	78.404	5.000	0.0640	-	2.146	9.970
	83.968	88.064	Band	98.230	10.000	0.1325	-	1.932	8.973
88.064	93.184	Band+BB	48.621	28.964	0.1944	1.337	6.212	-	
GRB090902B	-2.048	5.120	mBB	5.000	-0.012	0.0481	-	2.610	12.125
	5.120	8.192	mBB	6.346	-0.064	0.0137	2.856	13.266	61.577
	8.192	10.240	mBB	4.951	-0.574	0.0380	-	2.101	9.757
	10.240	13.312	mBB	20.000	-1.147	0.0482	2.471	11.480	53.284
	13.312	16.384	mBB	10.000	-0.752	0.0423	1.081	5.019	23.314
	16.384	19.456	mBB	5.000	-0.775	0.0509	-	1.846	8.575
	19.456	22.528	mBB	28.219	-0.975	0.0891	1.992	9.253	-
GRB090926A	-2.048	4.096	Band	759.906	5.000	0.0572	-	1.826	8.480
	4.096	7.168	Band	198.750	5.000	0.0357	-	2.657	12.340
	7.168	10.240	Band	230.006	10.000	0.0834	-	2.334	10.843
	10.240	13.312	Band	187.977	10.000	0.1064	-	1.829	8.496
GRB091003A	-2.048	10.240	Band	680.186	5.000	0.1635	-	-	3.758
	10.240	20.480	Band	288.675	29.303	0.0852	3.819	17.740	-
GRB091127A	-2.048	2.048	Band	46.689	10.000	0.0250	4.944	22.963	106.585
	2.048	8.192	Band	19.917	5.000	0.0704	-	3.272	15.197
GRB100414A	-2.048	10.240	CPL	975.324	5.000	0.0821	-	1.530	7.106
	10.240	18.432	CPL	1730.237	5.000	0.0740	-	1.541	7.159
	18.432	25.600	CPL	2047.803	5.000	0.1245	-	-	3.506

Burst Name	Start Time($T_0 + s$)	End Time($T_0 + s$)	Fit Model	E_{peak} (keV)	kT (keV)	f_{th}	$1 + \sigma_0$		
							$r_{0,1}^1$	$r_{0,2}^1$	$r_{0,3}^1$
GRB100728A	-2.048	22.528	CPL	4287.280	5.000	0.2388	-	-	2.680
	22.528	48.128	CPL	4288.484	5.000	0.2873	-	-	2.228
	48.128	61.440	CPL	957.657	10.000	0.4029	-	-	2.441
	61.440	73.728	CPL	1005.259	10.000	0.4366	-	-	2.043
	73.728	82.944	CPL	230.883	5.000	0.1261	-	-	4.186
	82.944	91.136	CPL	932.038	5.000	0.1321	-	-	3.996
	91.136	102.400	CPL	411.993	20.000	0.4897	-	1.023	4.750
	102.400	117.760	CPL	173.773	10.000	0.4936	-	-	2.195
	117.760	132.096	CPL	280.561	10.000	0.5062	-	-	1.942
	132.096	146.432	CPL	185.942	5.000	0.2339	-	-	3.016
	146.432	171.008	CPL	4288.458	5.000	0.3292	-	-	1.944
171.008	186.368	CPL	163.816	10.000	0.3202	-	-	4.524	
GRB100814A	-2.048	17.408	CPL+BB	222.629	30.438	0.4026	-	3.598	-
GRB100906A	-2.048	12.288	Band	74.296	5.000	0.1849	-	-	2.855
GRB101213A	-2.048	18.432	Band	2485.779	5.000	0.2483	-	-	3.121
GRB101219B	-2.048	19.456	CPL	4286.129	5.000	0.2915	-	-	2.905
GRB110721A	-2.048	3.072	Band+BB	1334.871	34.419	0.0854	4.784	22.206	-
	3.072	10.240	Band	428.720	50.000	0.1595	4.376	-	-
GRB110731A	-2.048	5.120	Band+BB	192.040	47.753	0.2533	1.609	7.473	-
	5.120	9.216	Band	1094.638	5.000	0.1450	-	-	3.482
GRB111228A	-12.288	5.120	Band	13.423	5.000	0.2635	-	-	2.979
	12.288	54.272	Band	14.930	5.000	0.2000	-	1.370	6.365
GRB120119A	-2.048	14.336	Band	525.853	10.000	0.4796	-	-	2.051
	14.336	22.528	Band	95.258	5.000	0.1446	-	-	3.655
	22.528	36.864	Band	133.701	10.000	0.4273	-	-	2.796
GRB120326A	-7.168	9.216	Band	36.329	5.000	0.5097	-	-	1.037
GRB120624B	-2.048	13.312	Band	341.531	5.000	0.1411	-	-	4.141
GRB120707A	-2.048	12.288	CPL+BB	245.757	28.013	0.1208	2.492	11.574	-
	12.288	21.504	Band+BB	52.935	20.232	0.1653	-	4.368	-
	21.504	28.672	Band	116.720	5.000	0.1336	-	-	3.262
	28.672	34.816	Band	53.695	5.000	0.1193	-	-	3.654
	34.816	48.128	Band	32.675	5.000	0.3055	-	-	1.571
GRB120711A	48.128	72.704	Band	1801.327	5.000	0.0982	-	1.277	5.934
	72.704	80.896	Band	1351.595	5.000	0.1584	-	-	2.751
	80.896	90.112	Band	350.544	5.000	0.0019	44.793	207.915	-
	90.112	96.256	Band	2596.171	5.000	0.0597	-	1.733	8.050
	96.256	102.400	Band	2342.635	5.000	0.0623	-	1.659	7.708
	102.400	112.640	Band	1652.340	5.000	0.1987	-	-	2.416
GRB120716A	167.936	190.464	Band	115.188	5.000	0.3137	-	-	2.107
GRB120909A	22.528	59.392	CPL	4287.832	5.000	0.3488	-	-	2.298
GRB121128A	-2.048	15.360	Band	42.274	5.000	0.4014	-	-	1.213
GRB130427A	-2.048	2.048	Band+BB	363.389	24.066	0.0945	2.037	9.460	-
	2.048	4.096	Band	97.664	5.000	0.0527	-	2.572	11.948
	4.096	5.120	Band+BB	459.147	33.025	0.0771	1.897	8.814	-
	5.120	6.144	Band+BB	695.987	39.277	0.1016	1.447	6.722	-
	6.144	7.168	Band+BB	880.279	44.453	0.1132	1.401	6.510	-

GRB130427A

Burst Name	Start Time($T_0 + s$)	End Time($T_0 + s$)	Fit Model	E_{peak} (keV)	kT (keV)	f_{th}	$1 + \sigma_0$		
							$r_{0,1}^1$	$r_{0,2}^1$	$r_{0,3}^1$
	7.168	8.192	Band+BB	909.531	48.543	0.1168	1.497	6.955	–
	8.192	9.216	Band+BB	859.654	41.976	0.1053	1.421	6.598	–
	9.216	10.240	Band+BB	849.200	40.612	0.0889	1.701	7.902	–
	10.240	11.264	Band+BB	969.636	33.876	0.1075	1.108	5.149	23.897
	11.264	13.312	Band+BB	525.769	17.370	0.0911	–	4.191	19.469
	13.312	16.384	Band+BB	362.916	29.569	0.0611	5.270	24.459	–
	16.384	19.456	Band+BB	257.621	58.742	0.1308	4.602	–	–
GRB130518A	8.192	22.528	Band	358.915	5.000	0.0634	–	3.005	13.957
	22.528	25.600	Band	882.595	5.000	0.0722	–	1.339	6.220
	25.600	28.672	CPL+BB	426.850	36.026	0.0794	3.231	15.007	–
	28.672	33.792	CPL+BB	172.195	31.294	0.0775	3.815	17.721	–
	33.792	47.104	Band+BB	298.825	22.358	0.0959	3.432	15.941	–
GRB130610A	–52.224	–19.456	Band+BB	255.818	30.196	0.2863	2.106	–	–
	–19.456	4.096	CPL+BB	232.275	30.121	0.3713	1.303	6.051	–
GRB130702A	–2.048	13.312	CPL	4219.994	5.000	0.2732	–	1.122	5.214
GRB131011A	–2.048	18.432	CPL+BB	277.374	33.383	0.1411	3.533	16.413	–
GRB131105A	16.384	40.960	CPL	3380.661	5.000	0.1977	–	–	3.934
	79.872	110.592	CPL	355.126	5.000	0.3202	–	–	2.203
GRB131108A	–7.168	7.168	Band	934.715	5.000	0.1726	–	–	2.851
	7.168	20.480	Band	122.518	10.000	0.4831	–	–	1.898
GRB131231A	–2.048	14.336	Band	904.124	10.000	0.4109	–	–	3.327
	14.336	19.456	Band	873.872	10.000	0.4104	–	–	1.863
	19.456	22.528	Band	357.972	10.000	0.1123	–	1.960	9.103
	22.528	24.576	Band	233.810	10.000	0.0601	–	4.032	18.730
	24.576	27.648	Band	131.167	5.000	0.0446	–	2.648	12.298
	27.648	30.720	Band+BB	46.439	10.519	0.0730	1.028	4.777	22.172
	30.720	33.792	Band+BB	313.132	26.616	0.2115	–	4.112	–
33.792	38.912	Band	37.503	10.000	0.2922	–	–	3.500	
GRB140108A	74.752	89.088	Band	1019.830	5.000	0.1748	–	–	4.283
GRB140213A	–2.048	4.096	Band	170.056	10.000	0.2303	–	1.026	4.765
	4.096	8.192	Band	43.292	20.000	0.4561	–	–	4.257
	8.192	18.432	Band	34.041	5.000	0.2557	–	–	2.795
GRB140423A	–38.912	–21.504	CPL+BB	598.068	39.178	0.0318	14.142	65.641	–
	–21.504	–1.024	Band	2.309	10.000	0.0128	7.676	35.656	165.502
GRB140508A	–2.048	12.288	Band+BB	345.600	31.571	0.2286	1.132	5.257	–
GRB140512A	98.304	120.832	CPL	437.956	5.000	0.2413	–	–	2.941
	120.832	133.120	CPL	293.555	5.000	0.2356	–	–	2.481
GRB140801A	–2.048	7.168	Band	83.642	10.000	0.1393	–	2.251	10.457
GRB141028A	–7.168	13.312	Band	1040.886	5.000	0.1681	–	–	3.542
	13.312	19.456	Band	319.573	5.000	0.1203	–	–	4.492
	19.456	31.744	Band	112.096	5.000	0.2936	–	–	2.026
GRB141220A	–2.048	7.168	Band	156.070	10.000	0.2873	–	–	4.604
GRB150314A	–2.048	3.072	Band+BB	305.738	31.625	0.0836	2.567	11.925	–
	3.072	7.168	Band	162.641	20.000	0.1280	–	3.922	18.205
	7.168	14.336	Band	511.829	5.000	0.1753	–	–	2.484
	–2.048	8.192	Band	275.877	30.911	0.0526	7.640	35.462	–

GRB150403A

Burst Name	Start Time($T_0 + s$)	End Time($T_0 + s$)	Fit Model	E_{peak} (keV)	kT (keV)	f_{th}	$1 + \sigma_0$		
							$r_{0,1}^1$	$r_{0,2}^1$	$r_{0,3}^1$
	8.192	12.288	Band	672.910	5.000	0.0714	–	1.461	6.788
	12.288	17.408	Band	248.756	20.000	0.3460	–	1.205	5.600
	17.408	29.696	Band	188.314	10.000	0.3647	–	–	3.644
GRB150821A	19.456	26.624	Band	117.491	5.000	0.2246	–	–	2.339
	26.624	35.840	Band	277.098	5.000	0.2255	–	–	2.566
	35.840	44.032	Band	482.127	60.000	0.2473	2.726	–	–
	53.248	66.560	Band	105.527	5.000	0.4988	–	–	1.053
GRB151027A	–2.048	9.216	Band	278.333	43.259	0.1597	4.859	–	–
	45.056	109.568	CPL	2945.402	5.000	0.2663	–	–	3.822
GRB160509A	–2.048	10.240	CPL+BB	321.717	32.865	0.1208	3.236	15.032	–
	10.240	12.288	Band	343.113	20.000	0.4122	–	–	2.913
	12.288	14.336	Band	396.505	10.000	0.0408	1.253	5.814	27.008
	14.336	16.384	Band	209.444	20.000	0.1444	–	2.637	12.248
	16.384	18.432	Band	285.852	20.000	0.1329	–	2.864	13.303
	18.432	22.528	Band	200.546	20.000	0.3022	–	1.260	5.852
	22.528	30.720	Band	200.724	5.000	0.2293	–	–	2.338
GRB160625B	178.176	188.416	Band	3123.807	60.000	0.0837	8.116	–	–
	188.416	189.440	Band+BB	438.593	47.696	0.0621	3.351	15.564	–
	189.440	191.488	Band+BB	372.393	33.625	0.0578	2.783	12.927	–
	191.488	193.536	Band	471.893	5.000	0.0049	7.446	34.586	160.532
	193.536	194.560	Band+BB	368.194	24.159	0.0241	6.018	27.956	–
	194.560	196.608	Band+BB	317.493	29.021	0.0329	5.035	23.387	–
	196.608	198.656	Band+BB	280.552	17.902	0.0250	4.235	19.670	91.301
	198.656	199.680	Band+BB	373.748	18.802	0.0231	4.862	22.582	104.817
	199.680	200.704	Band	969.729	5.000	0.0009	51.755	240.226	1115.029
	200.704	202.752	Band+BB	520.856	27.101	0.0178	10.277	47.701	–
	202.752	204.800	Band	345.542	40.000	0.0184	20.683	96.000	–
	204.800	206.848	Band	246.471	5.000	0.0094	3.481	16.167	75.042
	206.848	209.920	Band	116.407	10.000	0.1109	–	1.914	8.892
214.016	222.208	Band	822.360	5.000	0.1938	–	–	2.728	
GRB160629A	15.360	28.672	Band	856.776	50.000	0.3694	1.647	–	–
GRB160804A	–24.576	0.000	Band	42.214	5.000	0.4480	–	–	1.577
GRB161117A	36.864	47.104	Band	93.733	10.000	0.5017	–	–	2.160
GRB170214A	–2.048	12.288	Band+BB	2389.995	32.918	0.0457	13.218	–	–
	12.288	20.480	Band	272.135	5.000	0.1597	–	–	3.105
	20.480	28.672	Band+BB	320.507	33.556	0.1446	2.390	11.102	–
	28.672	36.864	Band+BB	2413.741	32.896	0.0332	15.696	72.855	–
	36.864	44.032	Band+BB	340.073	46.585	0.1635	2.604	12.095	–
	44.032	50.176	Band+BB	1449.851	41.194	0.0998	4.009	18.621	–
	50.176	57.344	Band+BB	347.149	37.892	0.1337	2.686	12.477	–
	57.344	63.488	Band	1087.015	5.000	0.1337	–	–	3.367
	63.488	69.632	Band+BB	2152.000	31.548	0.0262	17.838	82.794	–
	69.632	76.800	Band	1900.238	5.000	0.0227	1.996	9.271	43.032
	107.520	128.000	Band	3580.956	5.000	0.3316	–	–	1.998
	128.000	137.216	CPL+BB	230.044	32.561	0.0987	3.959	18.387	–
	137.216	148.480	Band	3576.749	5.000	0.2901	–	–	1.883
	–2.048	22.528	Band	1142.968	5.000	0.2301	–	–	2.531

GRB170405A

Burst Name	Start Time($T_0 + s$)	End Time($T_0 + s$)	Fit Model	E_{peak} (keV)	kT (keV)	f_{th}	$1 + \sigma_0$		
							$r_{0,1}^1$	$r_{0,2}^1$	$r_{0,3}^1$
	22.528	34.816	Band	770.655	5.000	0.1888	–	–	2.801
	34.816	53.248	Band	66.028	5.000	0.1734	–	–	3.704
GRB171010A	–2.048	11.264	Band	113.691	5.000	0.2126	–	–	3.642
	11.264	15.360	Band	647.195	5.000	0.0537	–	3.105	14.422
	15.360	18.432	Band	142.542	5.000	0.0650	–	2.329	10.818
	18.432	20.480	Band	110.204	5.000	0.0212	1.866	8.669	40.237
	20.480	22.528	Band	131.231	5.000	0.0175	2.265	10.522	48.837
	22.528	25.600	Band	107.062	5.000	0.0226	1.755	8.151	37.832
	25.600	28.672	Band	102.489	5.000	0.0203	2.152	9.997	46.403
	28.672	30.720	Band	110.762	5.000	0.0282	1.275	5.916	27.480
	30.720	32.768	Band+BB	431.974	29.396	0.0524	5.025	23.340	–
	32.768	34.816	Band+BB	293.178	11.267	0.0411	1.831	8.507	39.486
	34.816	36.864	Band	147.281	5.000	0.0088	5.434	25.242	117.164
	36.864	38.912	Band	62.595	5.000	0.0240	1.652	7.672	35.610
	38.912	41.984	Band+BB	242.835	29.220	0.0934	3.286	15.263	–
	41.984	45.056	Band	62.341	5.000	0.0256	1.703	7.910	36.714
	45.056	48.128	Band	68.396	5.000	0.0215	2.032	9.440	43.816
	48.128	51.200	Band	41.361	10.000	0.0659	1.496	6.947	32.245
	51.200	54.272	Band	73.462	5.000	0.0327	1.211	5.620	26.106
	54.272	56.320	Band	165.010	5.000	0.0207	1.912	8.880	41.217
	56.320	58.368	Band+BB	428.130	10.484	0.0264	3.535	16.418	76.205
	58.368	60.416	Band+BB	238.891	8.453	0.0473	1.155	5.362	24.905
	60.416	63.488	Band	90.191	5.000	0.0225	1.760	8.174	37.942
	63.488	65.536	Band	86.954	5.000	0.0247	1.601	7.432	34.520
	65.536	67.584	Band	79.856	5.000	0.0144	3.027	14.060	65.261
	67.584	69.632	Band	85.106	5.000	0.0098	4.901	22.766	105.670
	69.632	71.680	Band	103.378	5.000	0.0121	3.974	18.458	85.677
	71.680	74.752	Band	65.037	20.000	0.0518	4.089	18.994	–
	74.752	77.824	Band+BB	234.017	29.523	0.1561	1.729	8.032	–
	77.824	81.920	Band+BB	195.867	25.349	0.1258	2.274	10.563	–
81.920	84.992	Band+BB	246.436	35.160	0.1327	2.830	13.144	–	
84.992	89.088	Band+BB	367.023	29.634	0.1105	3.545	16.466	–	
89.088	95.232	Band	43.240	5.000	0.1962	–	–	3.583	
110.592	118.784	Band	34.079	5.000	0.2292	–	–	3.380	
128.000	136.192	Band	29.093	5.000	0.1796	–	1.023	4.750	
136.192	144.384	Band	30.314	5.000	0.2910	–	–	2.415	
GRB180620B	–7.168	14.336	Band	113.441	5.000	0.4164	–	–	1.294
GRB180703A	–7.168	10.240	Band	305.096	26.586	0.0643	6.569	30.491	–
GRB180720B	–7.168	6.144	Band	1631.934	5.000	0.0736	–	1.937	8.995
	6.144	9.216	Band	2376.161	5.000	0.0272	1.024	4.752	22.072
	9.216	11.264	Band	2401.166	5.000	0.0238	1.171	5.438	25.258
	11.264	14.336	Band+BB	271.121	29.747	0.0449	5.487	25.487	–
	14.336	16.384	Band+BB	277.642	26.802	0.0361	5.455	25.336	–
	16.384	18.432	Band+BB	474.485	28.498	0.0276	7.891	36.627	–
	18.432	22.528	Band	133.121	5.000	0.0372	–	3.831	17.793
	26.624	29.696	Band	125.858	60.000	0.0784	8.937	–	–
	29.696	35.840	Band	817.507	5.000	0.0793	–	1.632	7.581

Burst Name	Start Time($T_0 + s$)	End Time($T_0 + s$)	Fit Model	E_{peak} (keV)	kT (keV)	f_{th}	$1 + \sigma_0$		
							$r_{0,1}^1$	$r_{0,2}^1$	$r_{0,3}^1$
	47.104	52.224	Band	650.776	10.000	0.2550	–	–	3.989
GRB180728A	–7.168	11.264	Band+BB	32.534	4.725	0.0782	1.183	5.495	25.504
	11.264	13.312	Band	62.686	5.000	0.0225	2.729	12.676	58.839
	13.312	17.408	Band	39.554	5.000	0.0805	–	3.906	18.145
GRB181020A	–2.048	6.144	Band	1330.896	5.000	0.1082	–	1.229	5.711
	6.144	12.288	Band	635.015	5.000	0.0805	–	1.651	7.668
GRB190114C	–2.048	1.024	CPL	664.801	10.000	0.0582	1.038	4.819	22.386
	1.024	2.048	CPL+BB	404.340	12.120	0.0095	8.628	40.078	186.027
	2.048	3.072	CPL	1095.919	60.000	0.0263	19.111	88.706	–
	3.072	4.096	Band+BB	676.468	12.187	0.0117	5.656	26.273	121.950
	4.096	6.144	CPL	639.452	20.000	0.0090	19.249	89.346	–
	6.144	11.264	CPL	4290.623	60.000	0.2884	2.112	–	–
	11.264	17.408	Band+BB	241.065	13.750	0.0847	1.718	7.980	–
	17.408	22.528	CPL	32.926	5.000	0.1774	–	–	3.579
GRB190324A	–2.048	23.552	Band	140.940	10.000	0.5164	–	–	2.132
	23.552	33.792	Band	72.268	5.000	0.2236	–	–	2.911
GRB190829A	37.888	53.248	Band	8.944	5.000	0.2099	–	2.303	10.696
	53.248	59.392	Band	12.306	5.000	0.1160	–	4.594	21.322
GRB200524A	–2.048	8.192	Band+BB	4007.341	22.658	0.0917	2.642	12.272	–
	8.192	21.504	Band+BB	375.375	17.078	0.0830	2.664	12.374	–
GRB200613A	–2.048	7.168	Band	108.873	10.000	0.2856	–	–	4.228
	7.168	12.288	Band	71.854	10.000	0.3125	–	–	2.890
	12.288	16.384	Band	101.548	20.000	0.3052	–	1.507	6.998
GRB200826A	0.000	0.500	CPL+BB	151	23.666	0.0015	759.355	–	–
GRB200829A	–2.048	18.432	Band	302.776	5.000	0.1814	–	–	2.665
	18.432	20.480	Band+BB	359.650	32.662	0.0745	1.760	8.174	–
	20.480	23.552	Band+BB	378.778	27.293	0.0863	1.452	6.746	31.313
	23.552	38.912	Band+BB	120.767	29.659	0.1125	3.761	17.471	–
GRB201020B	–2.048	10.240	CPL+BB	591.720	22.627	0.1547	1.329	6.174	–
	10.240	17.408	Band	57.741	10.000	0.2761	–	–	3.496
GRB201104C	–2.048	27.648	Band	2.067	5.000	0.3917	–	–	2.234
GRB201216C	–7.168	8.192	Band	1226.549	5.000	0.0988	–	1.428	6.633
	8.192	12.288	Band	170.307	10.000	0.1504	–	1.440	6.691
	12.288	17.408	Band	110.066	5.000	0.0852	–	1.503	6.983
	17.408	21.504	Band	119.054	10.000	0.1512	–	1.433	6.655
	21.504	24.576	Band	127.093	10.000	0.1170	–	1.852	8.603
	24.576	26.624	Band	437.583	10.000	0.0555	–	4.304	19.994
	26.624	29.696	Band	353.328	5.000	0.0209	1.455	6.755	31.375
	29.696	34.816	Band	79.439	10.000	0.2306	–	1.035	4.808
GRB210204A	178.176	192.512	Band	157.621	5.000	0.2408	–	–	2.451
	192.512	200.704	Band	59.173	5.000	0.2732	–	–	1.617
	200.704	204.800	Band	57.457	10.000	0.3064	–	–	2.688
	210.944	217.088	Band	45.935	5.000	0.2300	–	–	1.920
	217.088	223.232	Band	47.216	5.000	0.2626	–	–	1.682
GRB210610B	–2.048	26.624	mBB	190.347	–0.134	0.2101	–	–	2.821
	26.624	32.768	mBB	951.700	–0.276	0.1121	–	–	3.591
	32.768	39.936	mBB	344.822	–0.151	0.2875	–	–	2.876

Burst Name	Start Time($T_0 + s$)	End Time($T_0 + s$)	Fit Model	E_{peak} (keV)	kT (keV)	f_{th}	$1 + \sigma_0$		
							$r_{0,1}^1$	$r_{0,2}^1$	$r_{0,3}^1$
	39.936	48.128	mBB	112.503	-1.882	0.1677	-	-	2.645
	48.128	60.416	mBB	68.578	-1.547	0.4964	-	-	2.020
GRB210704A	-7.168	4.096	CPL	659.428	5.000	0.1841	-	-	2.624
GRB211018A	-2.048	9.216	Band	397.962	10.000	0.4916	-	-	1.889
	9.216	19.456	Band	269.487	5.000	0.1661	-	-	3.642
	34.816	49.152	Band	1093.520	5.000	0.1905	-	-	3.177
	49.152	60.416	Band	1171.723	5.000	0.1814	-	-	3.025
	74.752	82.944	Band	1511.188	5.000	0.1275	-	-	4.307
	82.944	92.160	Band	689.554	5.000	0.1526	-	-	3.600
GRB211023A	61.440	66.560	Band	55.644	5.000	0.2053	-	-	2.382
	66.560	71.680	Band	55.427	20.000	0.1872	-	4.026	-
	83.968	89.088	Band	26.582	5.000	0.1106	-	1.546	7.180
GRB211211A	-2.048	3.072	Band+BB	305.909	32.429	0.0521	12.063	-	-
	3.072	5.120	Band+BB	481.812	23.429	0.0734	3.336	15.497	-
	5.120	6.144	Band+BB	404.987	25.219	0.0723	3.579	16.623	-
	6.144	7.168	Band+BB	862.219	33.844	0.1160	2.215	10.288	-
	7.168	9.216	Band+BB	939.338	28.202	0.0910	2.706	12.568	-
	9.216	11.264	Band+BB	243.001	11.269	0.0654	2.106	9.780	-
	11.264	16.384	Band	61.088	5.000	0.0793	-	3.769	17.508
	16.384	18.432	Band	91.632	20.000	0.1148	2.244	10.424	-
	18.432	20.480	Band+BB	123.170	17.379	0.0978	2.151	9.991	-
	20.480	22.528	Band	83.240	5.000	0.0232	3.058	14.203	65.924
	22.528	24.576	Band	101.978	5.000	0.0191	3.724	17.300	80.298
	24.576	27.648	Band+BB	370.581	31.578	0.0973	6.003	-	-
	31.744	35.840	Band	45.842	5.000	0.1482	-	1.662	7.722
	35.840	39.936	Band+BB	309.212	35.714	0.0874	10.366	-	-
51.200	59.392	Band	30.446	5.000	0.2744	-	1.090	5.062	
GRB220101A	93.184	102.400	Band	310.882	10.000	0.4839	-	-	1.995
	102.400	110.592	Band	463.488	5.000	0.1403	-	-	4.485
	110.592	119.808	Band	166.610	5.000	0.1579	-	-	4.387
GRB220107A	-2.048	10.240	Band	256.505	5.000	0.2435	-	-	2.189
GRB220527A	-2.048	4.096	Band	93.833	60.000	0.1453	4.512	-	-
	4.096	7.168	Band	97.901	5.000	0.0311	-	4.294	19.946
	7.168	11.264	Band+BB	221.878	34.365	0.2607	-	3.611	-
	11.264	23.552	Band	843.126	5.000	0.2946	-	-	2.103
GRB220627A	34.816	59.392	Band	369.824	5.000	0.2217	-	-	3.761
	82.944	101.376	Band	196.188	5.000	0.3484	-	-	1.789
	124.928	147.456	Band	1797.749	10.000	0.5087	-	-	2.284
	147.456	161.792	Band	261.076	10.000	0.4308	-	-	2.697
	161.792	178.176	Band	5000.000	30.000	0.0005	-	-	-

¹ σ_0 is constrained in different r_0 , the unit of r_0 is cm. As we mentioned in 2, we choose 10^8 , 10^9 and 10^{10} corresponding to the three different r_0 value in table: $r_{0,1}$, $r_{0,2}$ and $r_{0,3}$.

Table 2. Non-dissipation regime criteria

Regime	Criteria
Regime II $\eta > (1 + \sigma_0)^{1/2}$ $r_c > r_{ph} > r_{ra}$	$14.8(1+z)^{1/4} \left(\frac{kT_{ob}}{50keV}\right)^{1/4} \left(\frac{F_{BB}}{10^{-8}erg\ s^{-1}cm^{-2}}\right)^{3/16} r_{0,9}^{1/8} f_{th,-1}^{1/2} f_{\gamma}^{1/2} d_{L,28}^{3/8} > 1$ $0.24(1+z)^{-3} \left(\frac{kT_{ob}}{50keV}\right)^{-3} \left(\frac{F_{BB}}{10^{-8}erg\ s^{-1}cm^{-2}}\right)^{3/4} r_{0,9}^{-3/2} d_{L,28}^{3/2} > 1$ $1.43 \times 10^{-5} (1+z)^{-7} \left(\frac{kT_{ob}}{50keV}\right)^{-7} \left(\frac{F_{BB}}{10^{-8}erg\ s^{-1}cm^{-2}}\right)^{7/4} r_{0,9}^{-7/2} f_{th,-1}^3 f_{\gamma}^3 d_{L,28}^{7/2} < 1$
Regime III $\eta > (1 + \sigma_0)^{1/2}$ $r_{ph} > r_c$	$8.28(1+z)^{-3/2} \left(\frac{kT_{ob}}{30keV}\right)^{-3/2} \left(\frac{F_{BB}}{10^{-7}erg\ s^{-1}cm^{-2}}\right)^{5/8} r_{0,9}^{-1} f_{th,-1}^{5/4} f_{\gamma}^{5/4} d_{L,28}^{5/4} > 1$ $9.42 \times 10^{-2} (1+z)^{-14/3} \left(\frac{kT_{ob}}{30keV}\right)^{-14/3} \left(\frac{F_{BB}}{10^{-7}erg\ s^{-1}cm^{-2}}\right)^{7/6} r_{0,9}^{-7/3} f_{th,-1}^2 f_{\gamma}^2 d_{L,28}^{7/3} > 1$
Regime V $\eta < (1 + \sigma_0)^{1/2}$ $r_c > r_{ph} > r_{ra}$	$41.4(1+z)^{1/2} \left(\frac{kT_{ob}}{10keV}\right)^{1/2} \left(\frac{F_{BB}}{10^{-9}erg\ s^{-1}cm^{-2}}\right)^{3/8} r_{0,9}^{-1/4} f_{th,-1} f_{\gamma} d_{L,28}^{3/4} < 1$ $5.28(1+z)^{-3} \left(\frac{kT_{ob}}{10keV}\right)^{-3} \left(\frac{F_{BB}}{10^{-9}erg\ s^{-1}cm^{-2}}\right)^{3/4} r_{0,9}^{-3/2} d_{L,28}^{3/2} > 1$ $1.16 \times 10^{-5} (1+z)^{-8} \left(\frac{kT_{ob}}{10keV}\right)^{-8} \left(\frac{F_{BB}}{10^{-9}erg\ s^{-1}cm^{-2}}\right) r_{0,9}^{-3} f_{th,-1} f_{\gamma} d_{L,28}^2 < 1$
Regime VI $\eta < (1 + \sigma_0)^{1/2}$ $r_{ph} > r_c$	$8.28(1+z)^{-3/2} \left(\frac{kT_{ob}}{30keV}\right)^{-3/2} \left(\frac{F_{BB}}{10^{-7}erg\ s^{-1}cm^{-2}}\right)^{5/8} r_{0,9}^{-1} f_{th,-1}^{5/4} f_{\gamma}^{5/4} d_{L,28}^{5/4} < 1$ $5.63 \times 10^{-3} (1+z)^{-8/3} \left(\frac{kT_{ob}}{30keV}\right)^{-8/3} \left(\frac{F_{BB}}{10^{-7}erg\ s^{-1}cm^{-2}}\right)^{1/3} r_{0,9}^{-1} f_{th,-1}^{1/3} f_{\gamma}^{1/3} d_{L,28}^{2/3} > 1$